PHYSICAL REVIEW A **90**, 013806 (2014)

Analysis of a Veselago lens in the quasistatic regime

Asaf Farhi* and David J. Bergman†
Raymond and Beverly Sackler School of Physics and Astronomy, Faculty of Exact Sciences, Tel Aviv University, IL-6997801, Tel Aviv, Israel

(Received 26 April 2014; published 8 July 2014)

The resolution of conventional optical lenses is limited by the wavelength. Materials with a negative refractive index have been shown to enable the generation of an enhanced resolution image where both propagating and nonpropagating waves are employed. We analyze such a Veselago lens by exploiting some exact one-dimensional integral expressions for the quasistatic electric potential of a point charge in that system. These were recently obtained by expanding that potential in the quasistatic eigenfunctions of a three-flat-slabs composite structure. Numerical evaluations of those integrals, using realistic values for physical parameters like the electric permittivities of the constituent slabs and their thickness, reveal some surprising effects: For example, the maximum concentration of the electric field occurs not at the geometric optics foci but at the interfaces between the negative permittivity slab and the positive permittivity slabs. The analysis provides simple computational guides for designing such structures to achieve enhanced resolution of an optical image.

DOI: 10.1103/PhysRevA.90.013806 PACS number(s): 42.79.−e, 78.20.Bh, 42.70.−a

I. INTRODUCTION

The resolution limit in conventional optical imaging is known to be inversely proportional to the wavelength of the light. In 1967, a theoretical analysis by Veselago, based upon geometric optics, suggested that a flat slab with a negative refractive index can focus at a point the radiation from a point source [1]. At that time, materials possessing a negative refractive index did not exist, but recent developments in metamaterials have made the production of such materials possible [2–4]. In 2000, another important analysis by Pendry showed that materials with a negative refractive index can amplify evanescent waves, and thus enable the generation of an image by both propagating and nonpropagating waves, theoretically leading to unlimited resolution [5].

In the quasistatic regime, when the typical length scales are much smaller than the wavelength, Maxwell's equations reduce to static equations in which the electric and the magnetic fields are decoupled. Hence, the optical constant of relevance in this regime is the electric permittivity rather than the refractive index. The imaging of an electric point charge was recently analyzed by expanding the local electric potential in a series of the quasistatic eigenfunctions of a three-flat-slabs composite structure. This analysis yielded exact one-dimensional integral expressions for the quasistatic electric potential of a point charge in that system [6,7].

In this paper we first derive exact expressions for the electric field in a two-constituent three-flat-slabs composite structure in the form of one-dimensional integrals. These are obtained from the classical Maxwell equations in a continuous medium. The electromagnetic properties of that medium are characterized by a position and frequency-dependent but **k**-vector-independent electric permittivity. We further assume that this permittivity has a constant value in each constituent and changes discontinuously at any interface.

We then perform numerical computations for such a setup using realistic values for the physical parameters like the electric permittivities and the thickness of the intermediate slab. In these computations we vary both the location of the point charge and the constituent permittivities of the medium. These computations reveal surprising results among which is that the best imaging is obtained at the interfaces between the intermediate slab and the surrounding medium rather than at the geometric optics foci.

The structure of the paper is as follows. In Sec. II we present a summary of the basic theory for the analysis of such a setup. In Sec. III we derive exact expressions for the local electric field and validate our results. In Sec. IV we present results of the numerical computations for various charge locations and for various permittivity values. In Sec. V we discuss our results.

II. SUMMARY OF THE BASIC THEORY

In this section we describe the derivation of the exact results for the local electric potential field $\psi(\mathbf{r})$ in the quasistatic limit for the case of a point electric charge q in a two-constituent composite medium [6,7]. In these references a two-constituent composite structure, composed of three infinitely wide parallel slabs, is considered. The intermediate slab, with an electric permittivity ϵ_1, is placed between two slabs with an electric permittivity ϵ_2 (see Fig. 1).

In the static limit Maxwell's equations reduce to Poisson's equation for $\psi(\mathbf{r})$:

$$-4\pi\rho(\mathbf{r}) = \nabla\cdot(\epsilon_1\theta_1+\epsilon_2\theta_2)\nabla\psi, \tag{1}$$

which can be rewritten as

$$\nabla^2\psi = -4\pi\rho(\mathbf{r})/\epsilon_2 + u\nabla\cdot(\theta_1\nabla\psi), \tag{2}$$

$$\theta_1(\mathbf{r}) \equiv 1-\theta_2(\mathbf{r}) = \left\{\begin{matrix} 1 & \text{if} & \epsilon(\mathbf{r})=\epsilon_1, \\ 0 & \text{if} & \epsilon(\mathbf{r})=\epsilon_2, \end{matrix}\right\}, \quad u\equiv 1-\frac{\epsilon_1}{\epsilon_2},$$

where θ_1 and $\theta_2 \equiv 1-\theta_1$ are step functions that characterize the microstructure of the composite medium. The function $\rho(\mathbf{r})$ which appears in these equations represents a charge density distribution, including the possibility that $\rho(\mathbf{r}) = q\delta^3(\mathbf{r}-\mathbf{r}_0)$, i.e., a point charge at $\mathbf{r}_0$. The capacitor plates at $z=-L_2$ and $z=L_2'$ are included in order that the appropriate boundary

---

*asaffarhi@post.tau.ac.il
†bergman@post.tau.ac.il

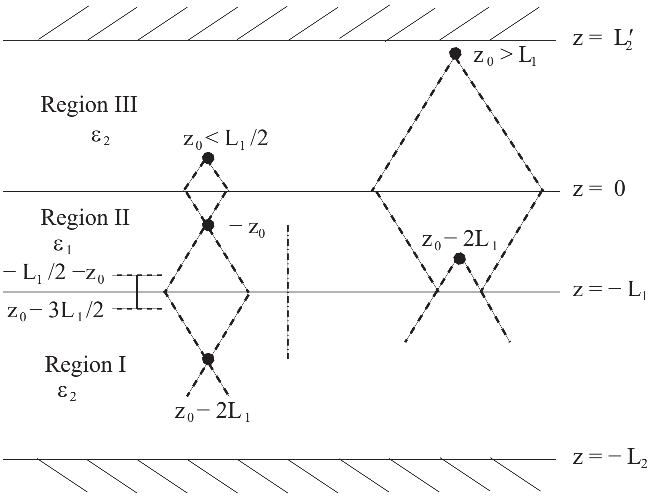

FIG. 1. A three-parallel-slabs microstructure that fills the entire volume of a large parallel-plate capacitor. The upper layer (Region III), where $\epsilon = \epsilon_2$, includes a point charge q located at $\mathbf{r}_0 = (0,0,z_0)$. In the left part $z_0 < L_1/2$ while in the right part $z_0 > L_1$, where L_1 is the thickness of the intermediate ϵ_1 layer (Region II). Even when all the other linear sizes of this structure tend to ∞, this configuration is still unsolvable in any simple fashion. The diagonal dashed lines show how a geometric optics or light rays description would lead to a focusing of the original point charge in Region III at new points in Regions I and II when $\epsilon_2 = -\epsilon_1$. The vertical dot-dashed line indicates the regions where $\psi(\mathbf{r})$ then diverges in the case shown on the left side, while the vertical solid line shows where the dissipation rate diverges (after Ref. [6]).

conditions may be imposed there so as to result in a unique solution for $\psi(\mathbf{r})$. At the end of the calculation we will take the limits $L_2 \to \infty$ and $L_2' \to \infty$.

We reformulate Eq. (2) as an integrodifferential equation for $\psi(\mathbf{r})$ [8]

$$\begin{aligned} \psi(\mathbf{r}) &= \psi_0(\mathbf{r}) + u\hat{\Gamma}\psi, \\ \hat{\Gamma}\psi &\equiv \int dV'\theta_1(\mathbf{r}')\nabla' G_0(\mathbf{r},\mathbf{r}')\cdot\nabla'\psi(\mathbf{r}'), \end{aligned} \tag{3}$$

where $G_0(\mathbf{r},\mathbf{r}')$ is Green's function for Laplace's equation with zero boundary conditions defined as follows:

$$\begin{aligned} &\nabla^2 G_0(\mathbf{r},\mathbf{r}') = -\delta^3(\mathbf{r}-\mathbf{r}'), \\ &G_0(\mathbf{r},\mathbf{r}') = 0 \quad \text{for} \quad z = -L_2 \quad \text{and} \quad z = L_2', \end{aligned}$$

and $\psi_0(\mathbf{r})$ is the solution of Poisson's equation in a uniform medium with a permittivity ϵ_2.

In the case of no charges and vanishing boundary conditions, Eq. (3) reduces to

$$s\psi(\mathbf{r}) = \hat{\Gamma}\psi, \quad s \equiv \frac{1}{u}.$$

Defining the scalar product of two scalar functions $\psi(\mathbf{r}),\phi(\mathbf{r})$ by

$$\langle\psi|\phi\rangle \equiv \int d^3r\,\theta_1\nabla\psi^*\cdot\nabla\phi$$

makes $\hat{\Gamma}$ a Hermitian operator [8]. Therefore it has a complete set of eigenfunctions ϕ_n and eigenvalues s_n

$$s_n\phi_n(\mathbf{r}) = \hat{\Gamma}\phi_n.$$

By using the expansion of the unity operator $\hat{I}$ in Eq. (3), we can expand the potential in a series of the eigenfunctions ϕ_n

$$\begin{aligned} \hat{I} &= \sum_n |\phi_n\rangle\langle\phi_n| \\ &\Longrightarrow \psi(\mathbf{r}) = \psi_0(\mathbf{r}) + \sum_n \frac{s_n}{s-s_n}\langle\phi_n|\psi_0\rangle\phi_n(\mathbf{r}). \end{aligned} \tag{4}$$

We now set the charge distribution to be that of a point charge located at $\mathbf{r}_0 = (0,0,z_0)$. This means that

$$\psi_0(\mathbf{r}) = \frac{q/\epsilon_2}{|\mathbf{r}-\mathbf{r}_0|}. \tag{5}$$

The eigenfunctions that satisfy Laplace's equation with vanishing boundary conditions are

$$\begin{aligned} &\phi_{\mathbf{k}}^{\pm}(\mathbf{r}) \\ &= e^{i\mathbf{k}\cdot\rho}\cdot\begin{cases} A_{\mathbf{k}}^{\pm}\sinh[k(z+L_2)], & z\in \text{I}, \\ B_{\mathbf{k}}^{\pm}\sinh(kz) + B_{\mathbf{k}}'^{\pm}\sinh[k(z+L_1)], & z\in\text{II}, \\ C_{\mathbf{k}}^{\pm}\sinh[k(z-L_2')], & z\in\text{III}. \end{cases} \end{aligned} \tag{6}$$

One might think that these eigenfunctions cease to be valid when $|\mathbf{k}|L_1$, $|\mathbf{k}|L_2$, $|\mathbf{k}|L_2'$ are not very small. That is not so: In fact, it is only necessary that Maxwell's equations for the local physical field $\mathbf{E}(\mathbf{r})$ be reducible, approximately, to Poisson's equation for the local electric potential field $\psi(\mathbf{r})$ [Eq. (1)]. The subsequent calculation of the eigenstates of the homogeneous version of that equation is a purely mathematical exercise and the resulting expansion of Eq. (4) for that approximate quasistatic physical potential field is exact. By imposing continuity of the potential and the perpendicular component of $\mathbf{D}$, we get the eigenvalues and the coefficients in these expressions

$$s_{\mathbf{k}}^{\pm} = \frac{1 \mp e^{-kL_1}}{2}, \quad A_{\mathbf{k}}^{\pm} = -B_{\mathbf{k}}^{\pm}\frac{\sinh(kL_1)}{\sinh[k(L_2-L_1)]},$$

$$B_{\mathbf{k}}'^{\pm} = \mp B_{\mathbf{k}}^{\pm}, \quad C_{\mathbf{k}}^{\pm} = \pm B_{\mathbf{k}}^{\pm}\frac{\sinh(kL_1)}{\sinh(kL_2')}.$$

Note that in the above expression for $s_{\mathbf{k}}^{\pm}$ we already took the limits $L_2',L_2 \to \infty$. The normalization condition $\langle\phi_{\mathbf{k}}^{\pm}|\phi_{\mathbf{k}}^{\pm}\rangle = 1$ leads to

$$1 = 2kL_xL_y|B_{\mathbf{k}}^{\pm}|^2\sinh(kL_1)[\cosh(kL_1)\mp 1].$$

The eigenvalues have a single accumulation point at $s = 1/2$ which is therefore a very singular point of Eq. (4). That equation leads to the following expressions for the electric potential in the three regions in the form of one-dimensional integrals [6]

$$\begin{aligned} \psi &= \frac{4s(1-s)q}{\epsilon_2}\int_0^\infty dk\,J_0(k\rho)\,\frac{e^{-k(z_0-z)}}{e^{-2kL_1}-(2s-1)^2} \\ &= 4q\epsilon_1\int_0^\infty dk\,J_0(k\rho)\,\frac{e^{-k(z_0-z)}}{(\epsilon_2-\epsilon_1)^2e^{-2kL_1}-(\epsilon_2+\epsilon_1)^2} \quad \text{in I}, \end{aligned} \tag{7}$$

$$\begin{aligned}\psi &= \frac{2sq}{\epsilon_2}\int_0^\infty dk\, J_0(k\rho)\, e^{-k(z_0-z)}\frac{e^{-2k(z+L_1)}-2s+1}{e^{-2kL_1}-(2s-1)^2}\\ &= 2q\int_0^\infty dk\, J_0(k\rho)\, e^{-k(z_0-z)}\\ &\quad\times\frac{(\epsilon_2-\epsilon_1)e^{-2k(z+L_1)}-(\epsilon_2+\epsilon_1)}{(\epsilon_2-\epsilon_1)^2e^{-2kL_1}-(\epsilon_2+\epsilon_1)^2}\ \text{in II,}\end{aligned} \tag{8}$$

$$\begin{aligned}\psi &= \psi_0+\frac{q(2s-1)/\epsilon_2}{\sqrt{\rho^2+(z+z_0)^2}}-\frac{4s(1-s)(2s-1)q}{\epsilon_2}\\ &\quad\times\int_0^\infty dk\, J_0(k\rho)\,\frac{e^{-k(z_0+z)}}{e^{-2kL_1}-(2s-1)^2}\\ &= \frac{q/\epsilon_2}{\sqrt{\rho^2+(z-z_0)^2}}\\ &\quad+\frac{\epsilon_2+\epsilon_1}{\epsilon_2-\epsilon_1}\frac{q/\epsilon_2}{\sqrt{\rho^2+(z+z_0)^2}}+4q\epsilon_1\frac{\epsilon_2+\epsilon_1}{\epsilon_2-\epsilon_1}\\ &\quad\times\int_0^\infty dk\, J_0(k\rho)\,\frac{e^{-k(z_0+z)}}{(\epsilon_2-\epsilon_1)^2e^{-2kL_1}-(\epsilon_2+\epsilon_1)^2}\ \text{in III.}\end{aligned} \tag{9}$$

These expressions for the potential, as well as the local dissipation rate, defined by $\mathrm{Im}(\epsilon)\,|\mathbf{E}|^2/8\pi$, were analyzed for the case of $s = 1/2$ (i.e., $\epsilon_1 = -\epsilon_2$) [6]. This analysis showed that the potential diverges in the range of positions $z_0 - 2L_1 < z < -z_0$. Moreover, when the location of the point charge satisfies $z_0 < L_1/2$, the local dissipation rate diverges for z in the range $[z_0 - 3L_1/2, -z_0 - L_1/2]$ (see Fig. 1).

When $s = 1/2$ these expressions for the potential take the following exact closed forms in those regions of z where it is nondiverging

$$\psi(\mathbf{r}) = \begin{cases} \frac{q/\epsilon_2}{\sqrt{\rho^2+(z-z_0+2L_1)^2}}, & \mathbf{r}\in \text{I},\\ \frac{q/\epsilon_2}{\sqrt{\rho^2+(z+z_0)^2}}, & \mathbf{r}\in \text{II},\\ \frac{q/\epsilon_2}{\sqrt{\rho^2+(z-z_0)^2}}, & \mathbf{r}\in \text{III}.\end{cases}$$

This means that the potential above the top geometric optics image at $\mathbf{r} = (0,0,-z_0)$ and below the bottom geometric optics image at $\mathbf{r} = (0,0,z_0 - 2L_1)$, is that of a point charge located at these points. In the intermediate z values between these expected images, the potential diverges (see Fig. 1). Since there are no point charges located at these points, the surface integration over the electric field perpendicular to an arbitrary envelope surrounding one of these points gives zero according to Gauss' law. This is fulfilled since the contribution to the surface integral from where the potential diverges cancels out with the contribution from where the potential is finite (for a spherical surface centered around one of these points, the first and second contributions give $-q/2$ and $q/2$, respectively).

III. EXACT EXPRESSIONS FOR THE ELECTRIC FIELD AND VERIFICATION OF THE RESULTS

We calculated exact expressions for the electric fields by differentiating the expressions for the potentials derived in Ref. [6] and reproduced in Eqs. (7) to (9) with respect to ρ and z. The expressions for the z and ρ components of $\mathbf{E}$ are as follows, where we substituted $s \equiv 1/2 + \Delta s$:

Region I

$$E_{\mathrm{I}\rho} = C_1\int_0^\infty dkkJ_1(k\rho)\frac{e^{-k(z_0-z)}}{e^{-2kL_1}-4(\Delta s)^2}, \tag{10}$$

$$E_{\mathrm{I}z} = -C_1\int_0^\infty dkkJ_0(k\rho)\frac{e^{-k(z_0-z)}}{e^{-2kL_1}-4(\Delta s)^2}, \tag{11}$$

where

$$C_1 \equiv \frac{q[1-4(\Delta s)^2]}{\epsilon_2}.$$

Region II

$$E_{\mathrm{II}\rho} = C_2\int_0^\infty dkkJ_1(k\rho)e^{k(z-z_0)}\frac{e^{-2k(z+L_1)}-2\Delta s}{e^{-2kL_1}-4(\Delta s)^2}, \tag{12}$$

$$E_{\mathrm{II}z} = C_2\int_0^\infty dkkJ_0(k\rho)e^{k(z-z_0)}\frac{e^{-2k(z+L_1)}+2\Delta s}{e^{-2kL_1}-4(\Delta s)^2}, \tag{13}$$

where

$$C_2 \equiv \frac{(1+2\Delta s)\,q}{\epsilon_2}.$$

Region III

$$\begin{aligned}E_{\mathrm{III}\rho} &= \frac{q}{\epsilon_2}\frac{\rho}{[\rho^2+(z-z_0)^2]^{3/2}}+\frac{2q\Delta s}{\epsilon_2}\frac{\rho}{[\rho^2+(z+z_0)^2]^{3/2}}\\ &\quad-2C_1\Delta s\int_0^\infty dkkJ_1(k\rho)\frac{e^{-k(z_0+z)}}{e^{-2kL_1}-4(\Delta s)^2},\end{aligned} \tag{14}$$

$$\begin{aligned}E_{\mathrm{III}z} &= \frac{q}{\epsilon_2}\frac{(z-z_0)}{[\rho^2+(z-z_0)^2]^{3/2}}+\frac{2q\Delta s}{\epsilon_2}\frac{(z+z_0)}{[\rho^2+(z+z_0)^2]^{3/2}}\\ &\quad-2C_1\Delta s\int_0^\infty dkkJ_0(k\rho)\frac{e^{-k(z_0+z)}}{e^{-2kL_1}-4(\Delta s)^2}.\end{aligned} \tag{15}$$

To verify the expressions for the potential and the electric field we checked the continuity of the potential and the perpendicular component of $\mathbf{D}$ at the interfaces. This was done by substituting $z = -L_1$ in the expressions for Regions I and II and $z = 0$ in the expressions for Regions II and III, yielding the same expressions in both cases (see the Appendix for more details).

IV. NUMERICAL COMPUTATIONS

We computed the one-dimensional integrals in the expressions for the potential and the electric field using MATLAB. We verified the computations of these integrals by checking the continuity of the potential and the perpendicular component of $\mathbf{D}$ at the interfaces for a set of ρ values (numerical values were compared). In addition, we calculated the field intensity $I(\mathbf{r})$ as well as the dissipation rate $W(\mathbf{r})$ in the three regions using the following definitions:

$$I(\mathbf{r}) \equiv |E_\rho(\mathbf{r})|^2 + |E_z(\mathbf{r})|^2, \tag{16}$$

$$W(\mathbf{r}) \equiv \mathrm{Im}[\epsilon(\mathbf{r})](|E_\rho(\mathbf{r})|^2 + |E_z(\mathbf{r})|^2). \tag{17}$$

These are in fact the expressions for the intensity and the dissipation in which $c/8\pi$ and $\omega/8\pi$ were not included, respectively, for simplicity.

We then placed another charge horizontally shifted from the original charge to find the charge separation that is needed for resolution of the images. We varied that separation until the field intensity at the midpoint between the two images was $1/e^{1/2}$ of the intensity at the images. We defined this distance as the separation distance needed to resolve the two images. To estimate the resolution in each horizontal layer we normalized the local intensity in Region I by dividing it by the intensity at the horizontal coordinates of the images in that layer (see Figs. 4, 7, 10, 13, 16).

Throughout the computations we used $q = e$, where e is the electron charge. We present the results for ψ, I, and W without specifying units. Thus, in order for those results to be in units of statV, erg/(s cm^2), and erg/(s cm^3), one has to multiply them by q/e, $q^2c/8\pi e^2$, and $q^2\omega/8\pi e^2$, respectively.

A. Polymethyl methacrylate-silver-photoresist setup for different vertical charge locations

We modeled a polymethyl methacrylate (PMMA)-silver-photoresist setup that is similar to the one used by the authors of Ref. [9] by a two constituents setup in which the two external slabs have the average permittivity value of PMMA and the photoresist, and the permittivity of the intermediate slab is that of metallic silver. We used the values for the permittivities suitable for a free-space wavelength of 365 nm [9]

$$\begin{aligned} \epsilon_{\text{silver}} &= -2.55 + 0.24i, \\ \epsilon_{\text{PMMA}} &= 2.25 + 0.12i, \\ \epsilon_{\text{PR}} &= 2.886 + 0.059i, \end{aligned}$$

which lead in the two constituents setup to the following permittivity values:

$$\epsilon_1 = -2.55 + 0.24i, \quad \epsilon_2 = 2.57 + 0.0896i.$$

The silver slab thickness was set to $L_1 = 35$ nm as in Ref. [9] and the external slabs in the calculation are assumed to have infinite thickness. We performed the computations for several locations of the point charge object on the vertical axis. The first location was $z_0 = 40$ nm $= 8L_1/7$ which agrees with the setup in Ref. [9]. We then placed the charge closer to the top interface at $z = 3L_1/4$ and $z = 3L_1/8$.

1. Charge located at $z_0 = 40\,\mathrm{nm} = 8L_1/7$

We first placed the charge at $z_0 = 40\,\mathrm{nm} = 8L_1/7$ as in Ref. [9]. In Fig. 2 we present the real and imaginary parts of the potential in all the regions. The potential is of course time dependent according to

$$\mathrm{Re}(\psi e^{i\omega t}) = \mathrm{Re}(\psi)\cos(\omega t) - \mathrm{Im}(\psi)\sin(\omega t).$$

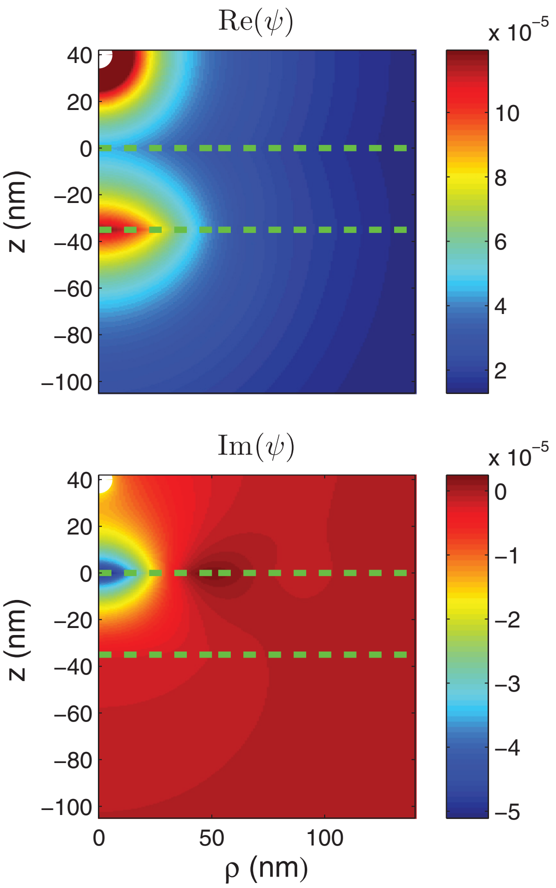

FIG. 2. (Color online) Real and imaginary parts of the potential for a charge located at $z_0 = 40\,\mathrm{nm} = 8L_1/7$.

The white circle denotes the object and, where applicable in the subsequent figures, the image expected according to geometrical optics. It can be seen that Re(ψ) has high values at the $z = -L_1$ interface and that Im(ψ) has high (absolute) values at the $z = 0$ interface. In this figure, as well as in subsequent figures that display all the regions, we used a linear color scale. To present an informative figure we mapped all the values higher than a certain value to this value. Thus, in all the locations which exhibit the highest value, the actual values are often much higher than the apparent value. In Fig. 3 we present the intensity and the dissipation in all the regions. It can be seen that the intensity is high at the interfaces and has a higher value at the bottom interface. The dissipation in Region II is higher than in Region I due to the fact that the imaginary part of the permittivity is higher in Region II. Note that the amplification of the electric field and the intensity starts even before the top interface. This adds to the picture described by the author of Ref. [5], where the amplification of the evanescent waves only in the silver slab was discussed.

In Fig. 4 we show the intensity and the horizontally normalized intensity in Region I for two horizontally displaced charges. It can be seen that the maximal resolution is at the interface $z = -L_1$. The distance between the charges that enables the images to be resolved as previously explained is 82.4 nm, which is in good agreement with the results found in Ref. [9] [see Fig. 4(d) there].

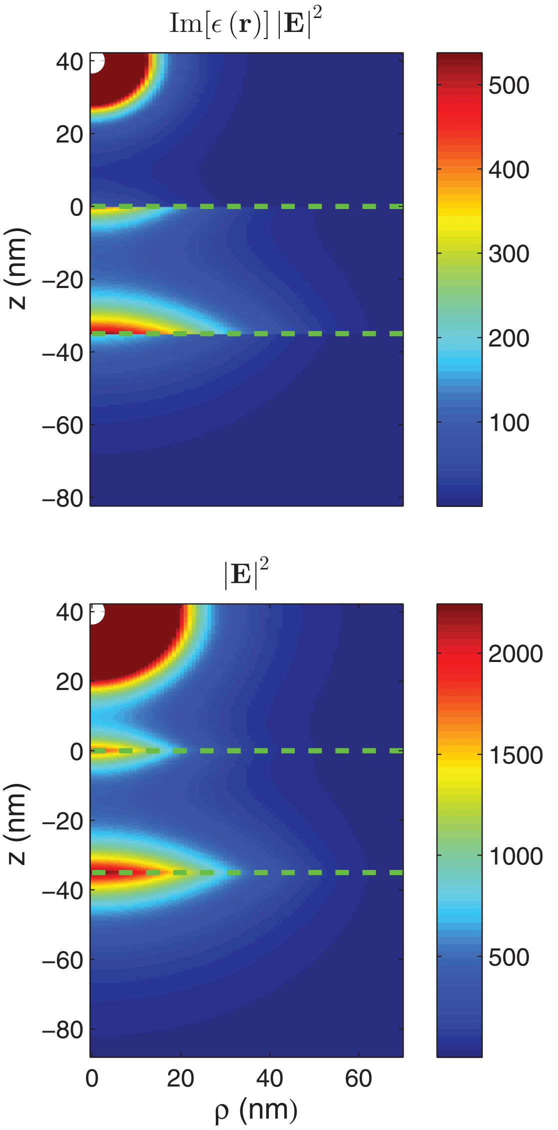

FIG. 3. (Color online) Intensity and dissipation for a charge located at $z_0 = 40\,\mathrm{nm} = 8L_1/7$.

2. *Charge located at $z_0 = 26.25\,\mathrm{nm} = 3L_1/4$*

In Fig. 5 we present the real and imaginary parts of the potential in all regions for a charge located at $z_0 = 26.25$ nm $= 3L_1/4$. Here also $\mathrm{Re}(\psi)$ and $\mathrm{Im}(\psi)$ (in absolute value) peak at the bottom and top interface, respectively.

In Fig. 6 we present the intensity and the dissipation in all regions. Here we originally expected that the intensity would have high values at the geometric optics foci $z = -3L_1/4$ and at $z = z_0 - 2L_1$. However, the intensity is actually concentrated at the $z = 0$ and $z = -L_1$ interfaces. In this case the peak intensity is higher at the top interface. The intensity in Region I is almost one order of magnitude higher than in the previous case.

In Fig. 7 the intensity and the horizontally normalized field intensity in Region I for two horizontally displaced charges are presented. The white circles denote the focal points. The separation exhibited is the smallest for which the images are still resolved as previously defined. Surprisingly, the separation of the images is best not at the expected focal plane but at the interface. Thus, both in terms of intensity and resolution the image formed at the interface $z = -L_1$ is optimal. In addition it can be seen that the separation distance in this case is 72 nm, which is better than the previous one.

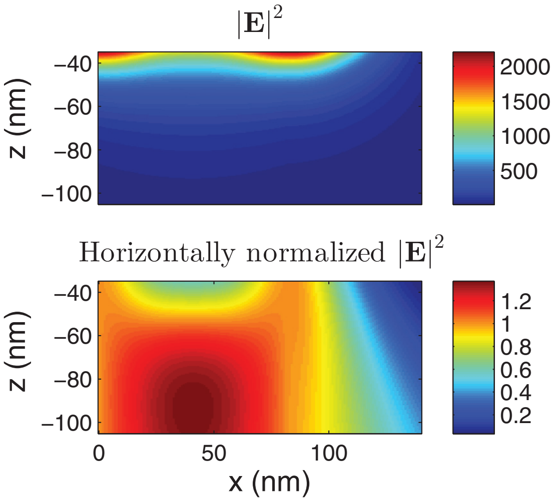

FIG. 4. (Color online) Intensity and horizontally normalized intensity in Region I for two charges located at $z_0 = 40\,\mathrm{nm} = 8L_1/7$, $x_1 = 0$, $x_2 = 82.4$ nm.

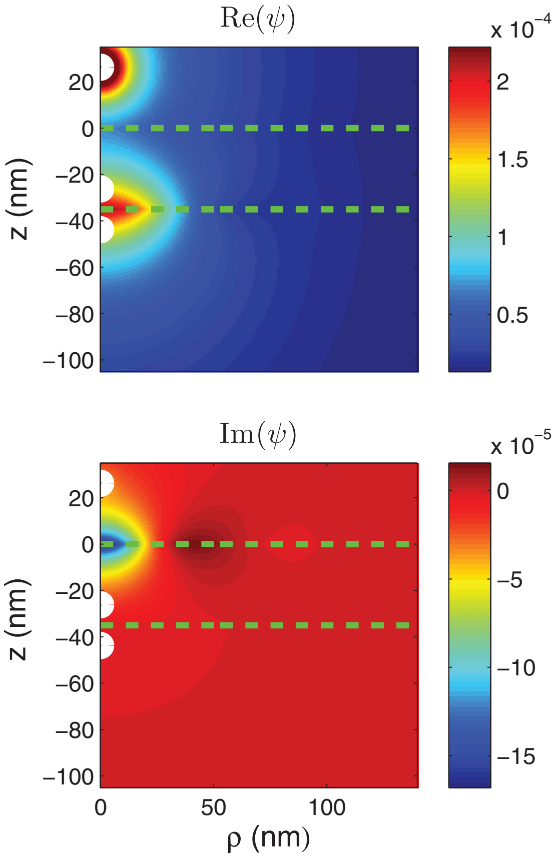

FIG. 5. (Color online) Real and imaginary parts of the potential for a charge located at $z_0 = 26.25\,\mathrm{nm} = 3L_1/4$.

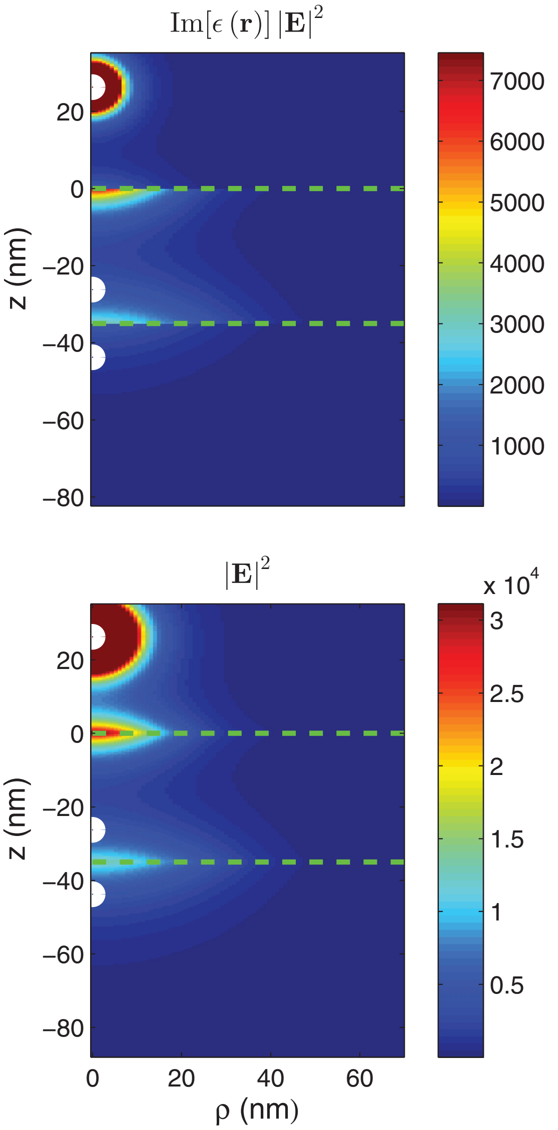

FIG. 6. (Color online) Intensity and dissipation for a charge located at $z_0 = 26.25\,\mathrm{nm} = 3L_1/4$.

3. *Charge located at* $z_0 = 13.125\,\mathrm{nm} = 3L_1/8$

Here we calculate the potential, intensity and dissipation for a setup with a charge located at $z_0 = 3L_1/8$. In this case if s were equal to half the dissipation rate should have diverged in the range $z_0 - 3L_1/2 < z < -z_0 - L_1/2$. However, since $s \neq 1/2$ we expect that the dissipation rate will increase in that range compared to the previous case where $z_0 = 3L_1/4$.

In Fig. 8 we present the real and imaginary parts of the potential for a charge located at $z_0 = 13.125\,\mathrm{nm} = 3L_1/8$. Here again $\mathrm{Re}(\psi)$ and $\mathrm{Im}(\psi)$ peak at the bottom and top interfaces, respectively.

In Fig. 9 we present the intensity and dissipation in the three regions. Here also the intensity is maximal at the interfaces rather than at the geometric optics foci. It can be clearly seen that the intensity is higher at the top interface. The intensity and the dissipation at the bottom interface in this case are almost one order of magnitude higher than in the previous case.

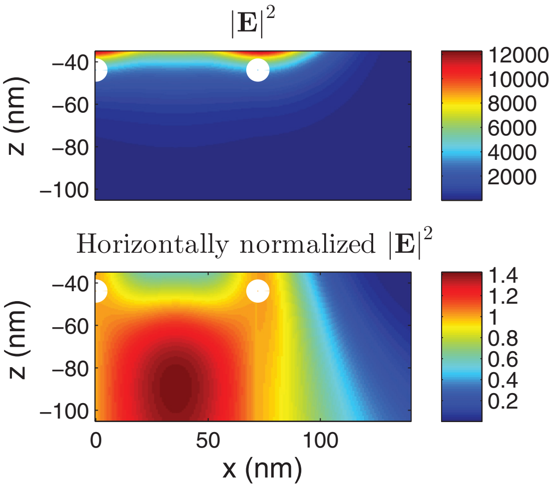

FIG. 7. (Color online) Intensity and horizontally normalized intensity in Region I for two charges located at $z_0 = 26.25\,\mathrm{nm} = 3L_1/4$, $x_1 = 0, x_2 = 72\,$ nm.

In Fig. 10 we present the intensity and the horizontally normalized intensity in Region I for two horizontally separated charges. It can be seen that the separation distance in this case is 63.2 nm which is better than in the previous cases.

It can be concluded that for the three object locations, the best images are formed at the interfaces. As we moved the

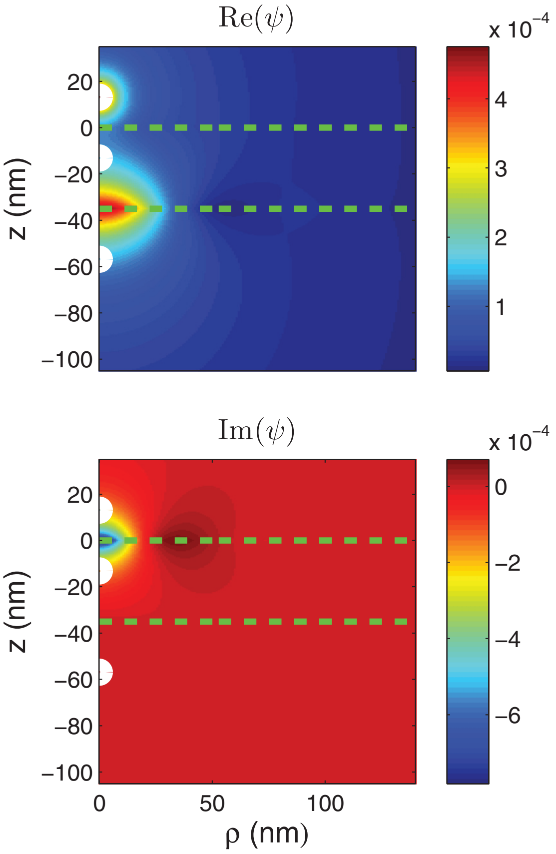

FIG. 8. (Color online) Real and imaginary parts of the potential for a charge located at $z_0 = 13.125\,\mathrm{nm} = 3L_1/8$.

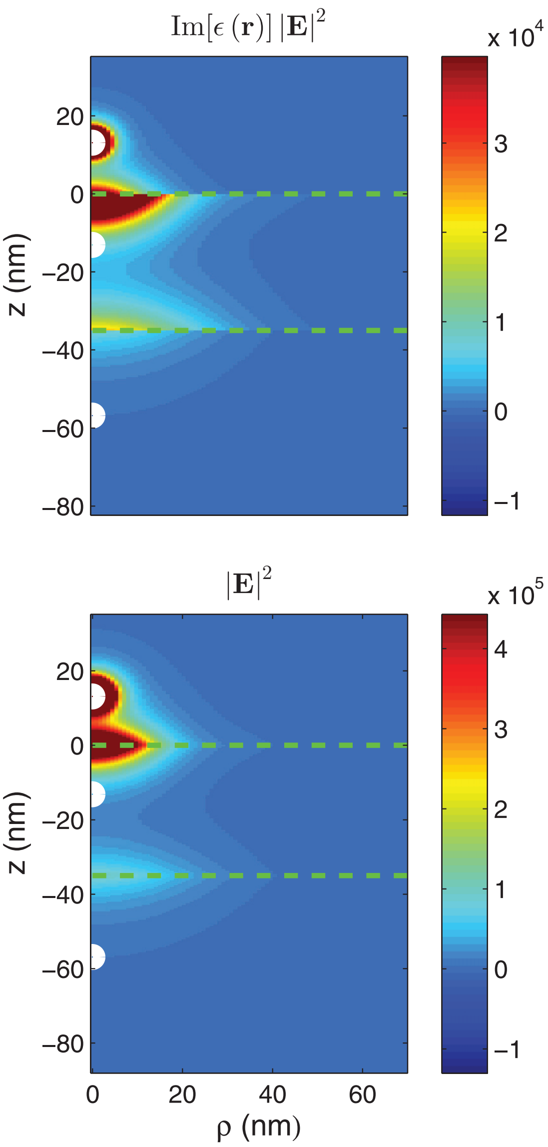
$\mathrm{Im}[\epsilon(\mathbf{r})]\,|\mathbf{E}|^2$

$|\mathbf{E}|^2$

FIG. 9. (Color online) Intensity and dissipation for a charge located at $z_0 = 13.125\,\mathrm{nm} = 3L_1/8$.

point charge closer to the $z = 0$ interface, the image formed at the $z = -L_1$ interface became better in terms of both intensity and resolution.

B. Computations for other permittivities

We repeated our computations for other values of s for a charge located at $z = 3L_1/4$. First, we performed computations with a setup in which the real part of Δs remained the same as in Sec. IV A and the imaginary part was divided by 100. Then, we performed a computation in which both the real and imaginary parts of Δs were divided by 100.

1. Δs *with* $\mathrm{Im}\,(\Delta s)$ *divided by* 100

In Fig. 11 $\mathrm{Re}(\psi)$ and $\mathrm{Im}(\psi)$ are presented. It can be seen that the potential now has an alternating sign as argued by the authors of Ref. [7]. In Fig. 12 the intensity and the dissipation are presented. The intensity at both interfaces is higher than in the PMMA-silver-photoresist setup. In addition the intensity here is higher at the bottom interface as opposed to the previous setup with $z_0 = 3L_1/4$, where it was higher at the top interface. The same is true regarding the local dissipation rates, despite the fact that $\mathrm{Im}(\Delta s)$ is smaller (which can be satisfied when

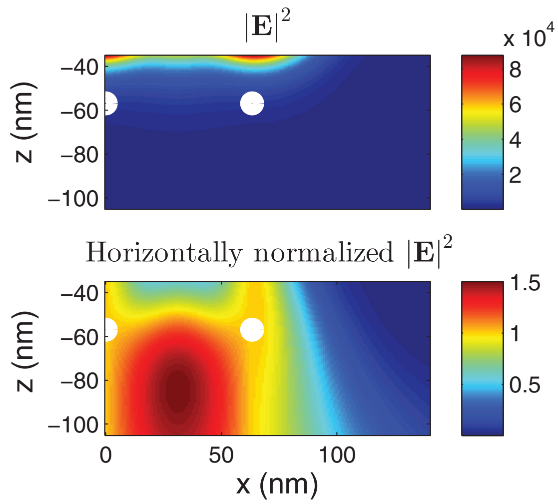
$|\mathbf{E}|^2$

Horizontally normalized $|\mathbf{E}|^2$

FIG. 10. (Color online) Intensity and horizontally normalized intensity in Region I for two charges located at $z_0 = 13.125\,\mathrm{nm} = 3L_1/8$, $x_1 = 0, x_2 = 63.2$ nm.

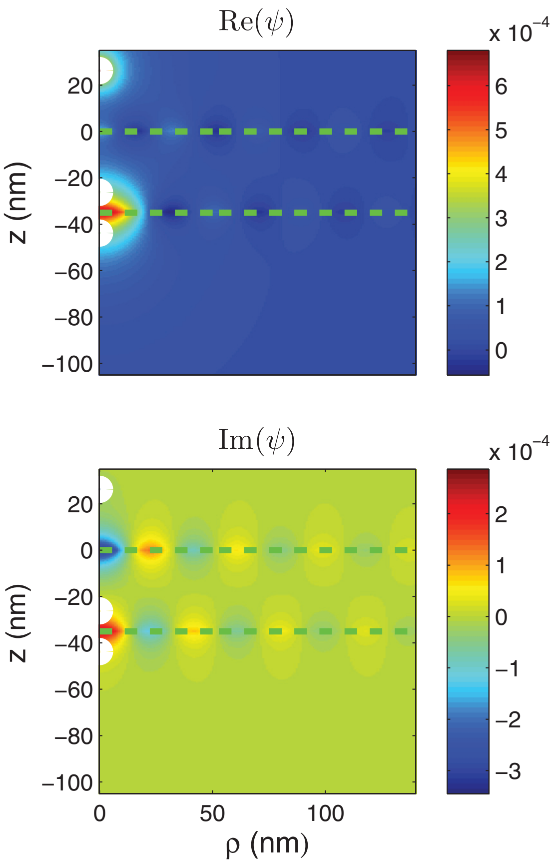
$\mathrm{Re}(\psi)$

$\mathrm{Im}(\psi)$

FIG. 11. (Color online) Real and imaginary part of the potential $z_0 = 3L_1/4$, $\Delta s = 0.0014 + 0.00032i$.

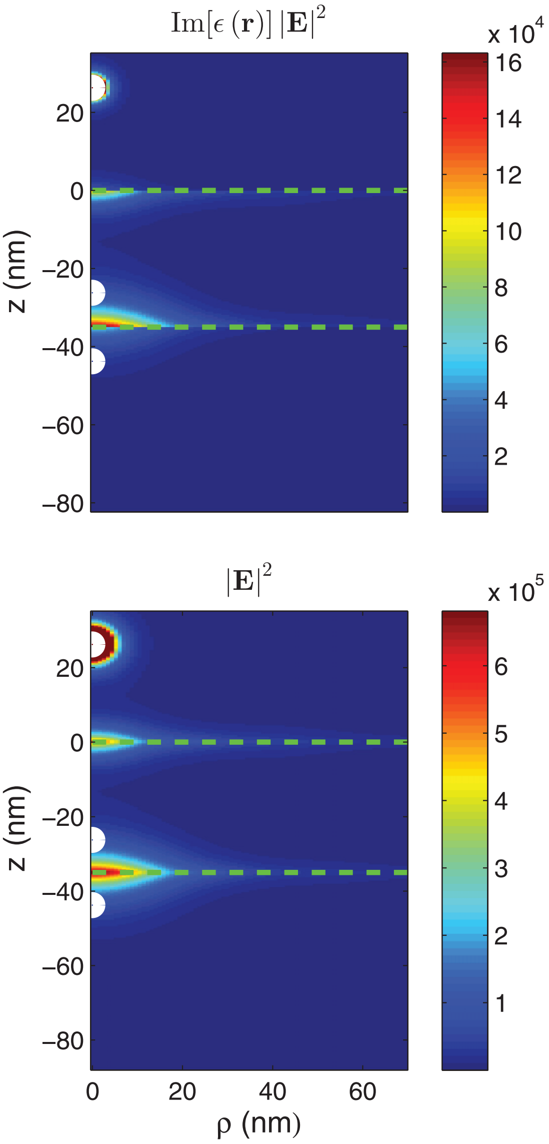

FIG. 12. (Color online) Intensity and dissipation for $z_0 = 3L_1/4$, $\Delta s = 0.0014 + 0.00032i$.

the imaginary part of the permittivity is small everywhere in the system). This is due to the fact that ψ and $\mathbf{E}$ tend to ∞ as $\Delta s \to 0$ only at the lower interface.

In Fig. 13 the intensity and the horizontally normalized intensity for two charges in Region I are presented. In this case the minimum separation distance between two objects for resolution of the images is 44.8 nm, which is significantly better than when $\mathrm{Im}(\Delta s)$ was not decreased by a factor of 100.

2. *Δs with both* $\mathrm{Re}\,(\Delta s)$ *and* $\mathrm{Im}\,(\Delta s)$ *divided by* 100

In Fig. 14 $\mathrm{Re}(\psi)$ and $\mathrm{Im}(\psi)$ are presented. They peak (in absolute value) at the bottom and top interfaces, respectively, and they have alternating signs. In Fig. 15 the intensity and dissipation for all the regions are presented. It can be seen that I and W at the bottom interface are higher compared to the case when we decreased just the imaginary part of Δs. In Fig. 16 the intensity and the horizontally normalized intensity in Region I for two separated charge objects are displayed.

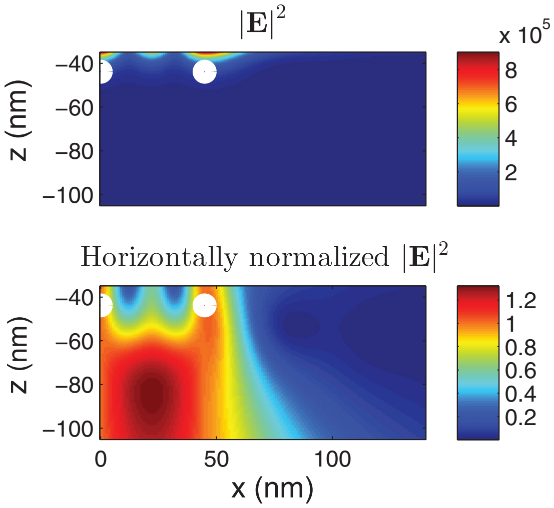

FIG. 13. (Color online) Intensity and horizontally normalized intensity for 2 charges $z_0 = 3L_1/4$, $x_1 = 0$, $x_2 = 44.8$ nm.

The minimum separation distance for this Δs value is 32 nm. It can be seen that when we also decrease $\mathrm{Re}(\Delta s)$ we have better separation between the images.

We can conclude that when the value of Δs is lowered, the optimal image locations are also at the interfaces. As we decrease the real and imaginary parts of Δs both the intensity

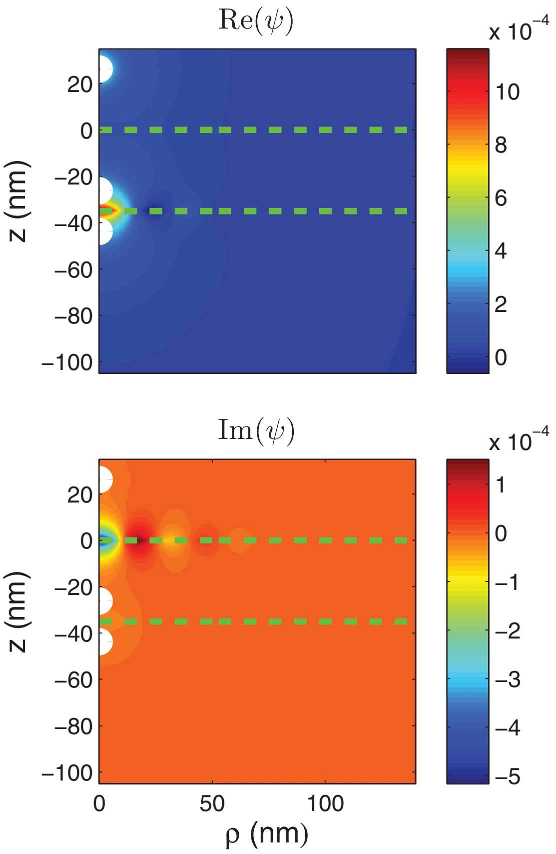

FIG. 14. (Color online) Real and imaginary part of the potential $z_0 = 3L_1/4$, $\Delta s = 0.000014 + 0.00032i$.

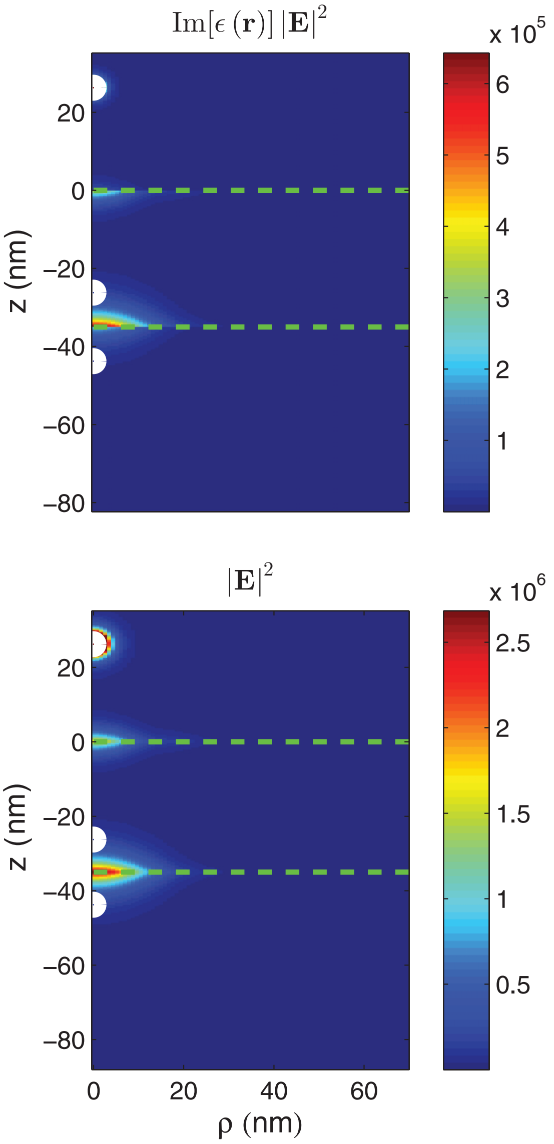

FIG. 15. (Color online) Intensity and dissipation for $z_0 = 3L_1/4$, $\Delta s = 0.000014 + 0.00032i$.

and the resolution become better for imaging. The analysis suggests that in the quasistatic regime for a setup with a small value of Δs, very high intensity and resolution can be reached (this occurs when $\epsilon_1 \approx -\epsilon_2$). It would be interesting to investigate whether such a pair of materials exists or can be engineered.

C. Analysis for a definite value of *k*

The expressions for the potential and the electric field can be easily decomposed into their k components. Thus, in Region II, the component associated with a specific $k = |\mathbf{k}|$ is simply the integrand in Eqs. (8), (12), and (13). Using this, we can easily calculate the contribution of each k component to the potential and the electric field.

It was interesting, in the case where $\Delta s \to 0$, to calculate the amplitude of the electric field for given ρ and k values at the top interface and compare it to the same quantity at the bottom interface. To that end we substituted $z = 0$ and $z = -L_1$ in the integrands of Eqs. (12) and (13) and took the limit $\Delta s \to 0$. This leads to the following results:

$$\frac{\lim_{\Delta s\to 0} E_{\mathrm{II}\,\rho}(z=-L_1)}{\lim_{\Delta s\to 0} E_{\mathrm{II}\,\rho}(z=0)} = \frac{C_2 k J_1(k\rho) e^{-z_0 k} e^{L_1 k}}{C_2 k J_1(k\rho) e^{-z_0 k}} = e^{L_1 k},$$

$$\frac{\lim_{\Delta s\to 0} E_{\mathrm{II}\,z}(z=-L_1)}{\lim_{\Delta s\to 0} E_{\mathrm{II}\,z}(z=0)} = \frac{C_2 k J_0(k\rho) e^{-z_0 k} e^{L_1 k}}{C_2 k J_0(k\rho) e^{-z_0 k}} = e^{L_1 k}.$$

These k-dependent ratios are the same as the transmission coefficient of the slab derived from the multiple scattering calculation in Ref. [5]. This is another confirmation of the validity of our results.

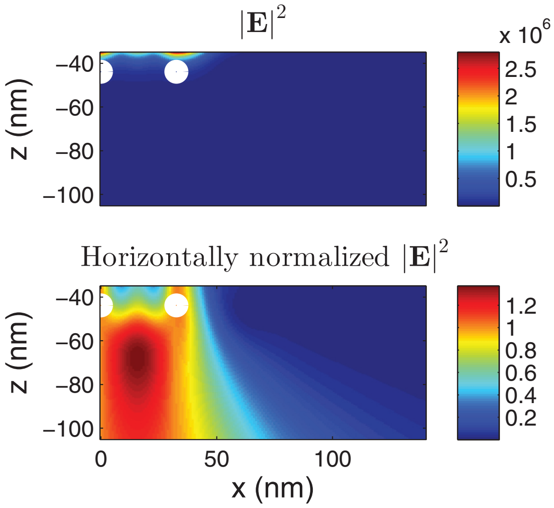

FIG. 16. (Color online) Intensity and horizontally normalized intensity in Region I for 2 charges $z_0 = 3L_1/4, x_1 = 0, x_2 = 32$ nm , $\Delta s = 0.000014 + 0.00032i$

V. DISCUSSION

We analyzed a two-constituents setup of three dielectric slabs, in which an electric point charge is located in the top slab. We first derived exact expressions for the local electric field in the form of one-dimensional integrals and verified our results. We then performed numerical computations of the electric potential, intensity, and dissipation for a setup that was previously tested in experiments. We calculated these quantities of interest for several charge locations and several permittivity values. Finally, we showed that our results agree with previous analytic results.

The computations reveal several important effects. The best images are formed at the interfaces between the slab and the surrounding medium rather than at the geometric optics foci. This optimality is in terms of both intensity and resolution. In addition the computations confirm previous analysis in which it was stated that the dissipation rate diverges when $\epsilon_1 = -\epsilon_2$. This can occur either when this quantity is real, in which case the constituents are free of any dissipation, or when they have imaginary parts with opposite signs. In the latter case one of the constituents exhibits dissipation while the other exhibits gain.

As was explained in that analysis, this counterintuitive effect originates from the fact that $s = 1/2$ is the accumulation point of all the eigenvalues and is therefore a very singular point of Maxwell's equations [6,7]. The computations for several charge locations show that when the object is closer to the interface with the intermediate slab, the imaging is better. The computations for several permittivity values show that as $\epsilon_1 \rightarrow -\epsilon_2$ the imaging becomes better.

APPENDIX: VERIFICATION OF THE ANALYTIC RESULTS

Calculations of $\psi(\mathbf{r})$ and $\mathbf{D}(\mathbf{r})$ at the two interfaces lead to

$$\psi_{\mathrm{I}}(z=-L_1) = \psi_{\mathrm{II}}(z=-L_1) = \frac{4qs(1-s)}{\epsilon_2} \int e^{k(-L_1-z_0)} \left[\frac{1}{e^{-2kL_1} - (1-2s)^2} \right] J_0(k\rho) dk, \tag{A1}$$

$$\psi_{\mathrm{II}}(z=0) = \psi_{\mathrm{III}}(z=0) = \frac{q(2\Delta s+1)}{\epsilon_2} \int_0^\infty dk J_0(k\rho) e^{-k(z_0)} \frac{e^{-2kL_1} - 2(\Delta s)}{e^{-2kL_1} - 4(\Delta s)^2}, \tag{A2}$$

$$\epsilon_1 E_{\mathrm{II}_z}(z=-L_1) = \epsilon_2 E_{\mathrm{I}_z}(z=-L_1) = \epsilon_1 \frac{4q\left(\frac{1}{2}+\Delta s\right)^2}{\epsilon_2} \int_0^\infty dk k J_0(k\rho) e^{k(-L_1-z_0)} \frac{1}{e^{-2kL_1} - 4(\Delta s)^2}, \tag{A3}$$

$$\epsilon_1 E_{\mathrm{II}_z}(z=0) = \epsilon_2 E_{\mathrm{III}_z}(z=0) = \epsilon_1 \frac{(1+2\Delta s)q}{\epsilon_2} \int_0^\infty dk k J_0(k\rho) e^{-kz_0} \frac{e^{-2kL_1} + 2\Delta s}{e^{-2kL_1} - 4(\Delta s)^2}, \tag{A4}$$

where we used $\frac{\epsilon_1}{\epsilon_2 - \epsilon_1} = \frac{\epsilon_1}{\epsilon_2}(\frac{1}{2} + \Delta s) = -(\frac{1}{2} - \Delta s)$ from the definition of s.

[1] V. Veselago, Usp. Fiz. Nauk **92**, 517 (1967) [Phys. Usp. **10**, 509 (1968)].

[2] D. F. Sievenpiper, M. E. Sickmiller, and E. Yablonovitch, Phys. Rev. Lett. **76**, 2480 (1996).

[3] J. B. Pendry, A. J. Holden, W. J. Stewart, and I. Youngs, Phys. Rev. Lett. **76**, 4773 (1996).

[4] J. B. Pendry, A. J. Holden, D. Robbins, and W. Stewart, IEEE Trans. Microwave Theory Tech. **47**, 2075 (1999).

[5] J. B. Pendry, Phys. Rev. Lett. **85**, 3966 (2000).

[6] D. J. Bergman, Phys. Rev. A **89**, 015801 (2014).

[7] D. J. Bergman and J. Ben Yakar, in *Proceedings of the SPIE Conference entitled "Plasmonics: Metallic Nanostructures and their Optical Properties XI"*, edited by M. I. Stockman, in the SPIE Meeting on Optics and Photonics, The San Diego Convention Center, San Diego, CA, August 2013 (SPIE, Bellingham, WA, 2013), p. 8809.

[8] D. J. Bergman, in *Les Méthodes de l'Homogénéisation: Théorie et Applications en Physiques*, edited by R. Dautray (Librairie Eyrolles, Paris, 1985), pp. 1–128.

[9] C. S. N. Fang, H. Lee, Cheng Sun, and X. Zhang, Science **308**, 534 (2005).